GEOPHYSICS, VOL. 84, NO. 2 (MARCH-APRIL 2019); P. C119–C128, 19 FIGS.
10.1190/GEO2018-0397.1

Image-domain wavefield tomography for VTI media

Vladimir Li[1], Antoine Guitton[2], Ilya Tsvankin[1], and Tariq Alkhalifah[3]

ABSTRACT

Processing algorithms for transversely isotropic (TI) media are widely used in depth imaging and typically bring substantial improvements in reflector focusing and positioning. Here, we develop acoustic image-domain tomography (IDT) for reconstructing VTI (TI with a vertical symmetry axis) models from P-wave reflection data. The modeling operator yields an integral wave-equation solution, which is based on a separable dispersion relation and contains only P-waves. The zero-dip NMO velocity (V_{nmo}) and anellipticity parameter η are updated by focusing energy in space-lag images obtained by least-squares reverse-time migration (LSRTM). Application of LSRTM helps mitigate aperture- and illumination-induced artifacts in space-lag gathers and improve the robustness of η-estimation. The impact of the trade-off between V_{nmo} and η is reduced by a three-stage inversion algorithm that gradually relaxes the constraints on the spatial variation of η. Assuming that the depth profile of the Thomsen parameter δ is known at two or more borehole locations, we employ image-guided interpolation to constrain the depth scale of the parameter fields and of the migrated image. Image-guided smoothing is also applied to the IDT gradients to facilitate convergence towards geologically plausible models. The algorithm is tested on synthetic reflection and borehole data from the structurally complicated elastic VTI Marmousi-II model. Although the initial velocity field is purely isotropic and substantially distorted, all three relevant parameters (V_{nmo}, η, and δ) are estimated with sufficient accuracy. The algorithm is also applied to a line from a 3D ocean-bottom-node data set acquired in the Gulf of Mexico.

INTRODUCTION

Reflection tomography, routinely used in prestack depth imaging, reconstructs the background velocity model by iteratively improving the consistency of migrated images. Whereas tomography conventionally operates with ray-based imaging algorithms (e.g., Kirchhoff migration), reverse time migration (RTM) is better suited for complex geologic models. Wavefield-based methods often employ an extended imaging condition to evaluate angle-dependent illumination (Rickett and Sava, 2002; Sava and Fomel, 2003). Estimation of residual energy at nonzero lags helps update the velocity model, which is commonly done using differential semblance optimization (DSO) or image-power operators (Symes and Carazzone, 1991; Zhang and Shan, 2013).

However, application of image-domain tomography (IDT) remains limited, primarily because extended images contain residual energy induced by not only velocity errors but also uneven illumination and insufficient acquisition aperture (Mulder, 2014; Dafni and Symes, 2016). As a result, velocity updates generated by the DSO operator are susceptible to illumination-related contamination. This issue is particularly relevant for η-estimation because energy focusing in the extended domain is less sensitive to this parameter compared to the zero-dip normal-moveout velocity V_{nmo} (Sava and Alkhalifah, 2012; Li et al., 2016a). Thus, robust η-inversion with IDT requires suppressing illumination and aperture-truncation artifacts in extended images (Li et al., 2017).

IDT algorithms can be improved by using a better designed penalty operator (Yang and Sava, 2015) or a more robust imaging condition (Lameloise et al., 2015; Chauris and Cocher, 2017; Hou and Symes, 2017). Illumination issues can also be mitigated with least-squares RTM (LSRTM), as done in migration-based traveltime tomography (MBTT) (Clément et al., 2001) and reflection waveform inversion (RWI; Hicks and Pratt, 2001; Pattnaik et al., 2016). In this paper,

Manuscript received by the Editor 22 May 2018; revised manuscript received 7 September 2018; published ahead of production 26 December 2018; published online 11 March 2019.
[1]Center for Wave Phenomena, Colorado School of Mines, Golden, Colorado, USA. E-mail: vli@mymail.mines.edu; ilya@mines.edu.
[2]Center for Wave Phenomena, Colorado School of Mines, Golden, Colorado, USA and DownUnder GeoSolutions, Denver, USA. E-mail: aguitton@gmail.com.
[3]King Abdullah University of Science and Technology, Thuwal, Saudi Arabia. E-mail: tariq.alkhalifah@kaust.edu.sa.

we employ LSRTM supplemented by nonstationary matching filters for gradient preconditioning (Guitton, 2017).

P-wave kinematics in VTI (TI with a vertical symmetry axis) media is governed by the Thomsen parameters V_{P0} (vertical velocity), ϵ, and δ or by V_{nmo}, η, and δ (Tsvankin, 2012). Because δ is poorly constrained by P-wave reflection moveout, robust VTI IDT algorithms require additional information typically provided by borehole data, such as check shots (Wang and Tsvankin, 2013a, 2013b). Li et al. (2016b) augment the DSO and image-power terms in the objective function with petrophysical constraints. Knowledge of the covariance between the model parameters mitigates parameter trade-offs but the results indicate that realistic errors in the covariance matrix may lead to insufficient model updates.

As demonstrated by Wang and Tsvankin (2013b), trade-offs between the parameters of tilted TI media in ray-based reflection tomography can be reduced by using a multistage inversion scheme that gradually relaxes spatial constraints on the anisotropy coefficients. Pattnaik et al. (2016) employ a similar approach in RWI to resolve the parameters V_{nmo} and η. Velocity model-building can also benefit from image-guided constraints (Hale, 2009a; Guitton et al., 2012; Ma et al., 2012). In particular, image-guided smoothing of the anisotropy coefficients (Wang and Tsvankin, 2013b; Li et al., 2016b) helps steer the inversion for TI media toward geologically plausible solutions.

In summary, existing anisotropic wave-equation-based image-domain tomographic algorithms do not properly account for illumination and aperture-truncation artifacts in extended images. Also, some of them employ tight constraints on the medium parameters obtained from a priori information. Here, we propose a nested LSRTM-based optimization algorithm for VTI media that addresses these issues. As mentioned above, application of LSRTM substantially reduces the magnitude of artifacts in the extended domain. Also, updates in the parameters V_{nmo} and η are driven by IDT (Li et al., 2017), whereas the δ-field is obtained from image-guided interpolation between boreholes. Similarly to Wang and Tsvankin (2013b), we gradually relax the image-guided smoothing constraints applied to the η-gradient.

We start by reviewing the wavefield-extrapolation algorithm and application of nonstationary matching filters to LSRTM in TI media. Then we discuss the IDT objective functions and describe a three-stage inversion algorithm designed to stabilize η-estimation. Next, matching filters are applied to extended RTM gathers for a simple layered VTI model. The results demostrate that these filters efficiently mitigate illumination-induced artifacts in the extended domain. Although the developed algorithm is acoustic, we test it on reflection and borehole data generated for the elastic VTI Marmousi-II model. Finally, processing of a line from the 3D ocean-bottom-node (OBN) data set acquired in the Gulf of Mexico demonstrates the feasibility of updating the η-field using the presented methodology.

METHODOLOGY

P-wave extrapolation operator in VTI media

Anisotropic wavefield extrapolation often employs the pseudoacoustic approximation (Alkhalifah, 1998, 2000), which can include different three-parameter sets (e.g., V_{P0}, ϵ, and δ or V_{nmo}, η, and δ). Integral wave-equation solutions compute the phase shift for pure P-mode extrapolation (time-stepping) using the dispersion relation (Fomel et al., 2013b; Du et al., 2014). Following Li et al. (2017), we use the separable dispersion relation described in Schleicher and Costa (2016):

$$\omega^2 = (1+2\epsilon)V_{P0}^2 k_x^2 + V_{P0}^2 k_z^2 - 2(\epsilon-\delta)V_{P0}^2 \frac{k_x^2 k_z^2}{k_x^2+k_z^2} \times \left[1 - 2\epsilon \frac{k_x^2}{k_x^2+k_z^2} + 2(\epsilon-\delta)\frac{k_x^2 k_z^2}{(k_x^2+k_z^2)^2}\right], \tag{1}$$

where k_x and k_z are the horizontal and vertical wavenumbers. Equation 1 is obtained from the 2D pseudoacoustic version (i.e., the version in which the S-wave velocity along the symmetry axis is set to zero) of equation 65 from Schleicher and Costa (2016). The Padé coefficients q_1 and q_2 in that equation are set to their theoretical values (1/2 and 1/4, respectively). The modeling operator for gradient computation is given in the weak-anellipticity (small η) approximation by

$$\mathbf{L}_{\text{INT}} = -\frac{\partial^2}{\partial t^2} - V_{\text{nmo}}^2 k_x^2 - \frac{V_{\text{nmo}}^2}{1+2\delta} k_z^2 - 2\eta V_{\text{nmo}}^2 \frac{k_x^4}{k_x^2+k_z^2}. \tag{2}$$

The corresponding adjoint operator has the form (Li et al., 2017)

$$\mathbf{L}_{\text{INT}}^{\dagger} = -\frac{\partial^2}{\partial t^2} - k_x^2 V_{\text{nmo}}^2 - k_z^2 \frac{V_{\text{nmo}}^2}{1+2\delta} - \frac{2k_x^4}{k_x^2+k_z^2}\eta V_{\text{nmo}}^2. \tag{3}$$

A more detailed discussion of this propagator can be found in Li et al. (2017).

Extended least-squares RTM with matching filters

Information about angle-dependent subsurface illumination contained in extended images can be used for velocity model-building. The general imaging condition is formulated as (Sava and Vasconcelos, 2009):

$$I(\mathrm{x}, \boldsymbol{\lambda}, \tau) = \sum_{e,t} W_s(\mathrm{x}-\boldsymbol{\lambda}, t-\tau) W_r(\mathrm{x}+\boldsymbol{\lambda}, t+\tau), \tag{4}$$

where $I(\mathrm{x}, \lambda, \tau)$ is the extended image, W_s and W_r denote the source and receiver wavefields, respectively, $\boldsymbol{\lambda}$ is the space lag, τ is the time lag, and e indicates summation over experiments (i.e., sources). Assuming perfect illumination and infinite bandwidth, imaging with the correct velocity model focuses events at zero lag. Therefore, energy defocusing in extended gathers provides information for velocity analysis.

However, algorithms designed to minimize residual energy in the extended domain must account for additional defocusing caused by uneven illumination and aperture truncation (Yang and Sava, 2015). Errors in the anisotropy coefficients often cause weaker defocusing compared to that due to velocity errors (Li et al., 2016a). Thus, it is critically important for anisotropic IDT to mitigate illumination-related artifacts before back-projecting image residuals, which can be achieved with nonstationary convolution filters. As shown by Guitton (2017), these filters provide a low-rank approximation to the true inverse Hessian and can be computed as:

$$\mathbf{m}_0 = \mathbf{R}^{\mathrm{T}}(\mathbf{d_r}, \mathbf{d_s}), \tag{5}$$

$$\mathbf{m}_1 = \mathbf{R}^{\mathrm{T}}\,\mathbf{R}\,\mathbf{m}_0, \tag{6}$$

$$\|\mathbf{m}_0 - \mathbf{B}\mathbf{m}_1\|^2 \approx 0, \tag{7}$$

where $\mathbf{m}_0$ is the RTM image, $\mathbf{R}^{\mathrm{T}}$ represents the sequence of wavefield-extrapolation and extended-imaging operators, $\mathbf{d}_r$ contains the recorded data, $\mathbf{d}_s$ is the source wavelet, $\mathbf{m}_1$ is the image obtained after demigration and migration (i.e., after the $\mathbf{R}^{\mathrm{T}}\mathbf{R}$ sequence), and $\mathbf{B}$ is the estimated nonstationary filter. Application of nonstationary matching filters involves the following steps:

- compute the "blurred" image by demigrating and migrating the RTM gathers (equation 6).
- estimate the "bank" of matching filters by solving equation 7 with the conjugate-gradient method.
- apply the filters $\mathbf{B}$ to the RTM image $\mathbf{m}_0$ to obtain the "pseudoinverse" image.

The matching filters computed with this approach substantially improve RTM extended gathers. Parameter estimation in structurally complex media can also benefit from applying this scheme to preconditioning of the LSRTM gradient (Guitton, 2017).

Objective function

Image-domain tomography is often based on residual-energy minimization with the DSO operator (Symes and Carazzone, 1991; Shen and Symes, 2008). An alternative approach is to maximize the zero-lag energy using the image-power (IP) criterion (Chavent and Jacewitz, 1995; Soubaras and Gratacos, 2007; Zhang and Shan, 2013). Robust VTI parameter estimation, however, is not feasible without additional constraints. Inversion driven by the DSO operator can produce significantly overestimated η-values, which "honor" the DSO criterion of small residuals. Whereas IP can update high model-wavenumber components, the corresponding objective function often has multiple local minima because the spatial positioning of such updates is controlled by the background velocity. The objective function can combine the DSO and IP criteria to increase the robustness of parameter estimation (Shan and Wang, 2013; Shan et al., 2014; Weibull and Arntsen, 2014; Li et al., 2016b):

$$\mathcal{J} = \mathcal{J}_{\mathrm{DSO}} + \alpha\,\mathcal{J}_{IP}, \tag{8}$$

where α is a model-dependent weighting factor. The adjoint-state gradients of the terms $\mathcal{J}_{\mathrm{DSO}}$ and $\mathcal{J}_{IP}$ for the wave-equation operator in equation 2 are derived in Li et al. (2017).

Multistage inversion algorithm

The complete workflow of the developped IDT algorithm is shown in Figure 1. An important part of the workflow is a three-stage model-updating algorithm designed to address the following issues that hamper VTI velocity analysis:

- simultaneous estimation of the parameters V_{nmo} and η is feasible only if the initial field of V_{nmo} (or V_{P0}) is sufficiently accurate.
- estimation of the parameter δ requires additional (e.g., borehole) information.
- high model-wavenumber components can be resolved only for accurate background velocity.

After obtaining LSRTM gathers, we construct the objective function using both the DSO and image-power terms (equation 8). It is convenient to invert for the dimensionless parameters $(V_{\mathrm{nmo}}/V_{\mathrm{nmo}}^{\mathrm{init}})^2$ ($V_{\mathrm{nmo}}^{\mathrm{init}}$ is the initial NMO velocity), $1+2\delta$, and $1+2\eta$, which are equal to unity for the initial isotropic model.

Whereas updates in V_{nmo} and η are driven by energy focusing in extended LSRTM gathers, the parameter δ is updated by image-guided interpolation between two (or more) boreholes, where the vertical δ-profile is assumed to be known. The interpolation is performed with the LSRTM image generated at the current iteration.

Similarly to Wang and Tsvankin (2013b), we design a three-stage inversion algorithm that gradually relaxes the constraints on the spatial variation of η. Because of the dominant influence of V_{nmo} on reflection moveout, errors in this parameter can bias η-estimation. Therefore, we update V_{nmo} and η sequentially, as proposed by Pattnaik et al. (2016) for purposes of reflection waveform inversion. The first inversion stage is designed to update only V_{nmo}, whereas the second stage (when the V_{nmo}-field is more accurate) is limited to updating η. Finally, at the third stage V_{nmo} and η are updated simultaneously. The weighting factor α in equation 8 is fixed for each stage and increases during the optimization process to assign a larger weight to the IP term as the model becomes more accurate.

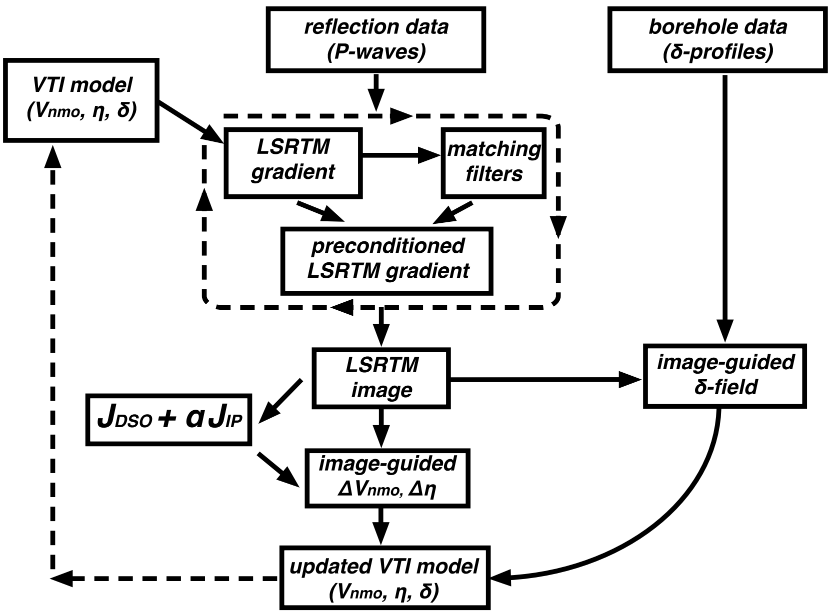

Figure 1 Workflow of the VTI image-domain tomographic algorithm. The inner loop performs least-squares reverse time migration (LSRTM) preconditioned with nonstationary matching filters. The extended LSRTM image is used to update the parameters V_{nmo} and η. A multistage inversion scheme is employed to reduce the trade-off between these parameters. The δ-field is obtained from image-guided interpolation between boreholes.

To steer the algorithm towards geologically plausible solutions, image-guided smoothing (Hale, 2009b) is applied to the V_{nmo}- and η-gradients (Guitton et al., 2012; Wang and Tsvankin, 2013b; Li et al., 2016b). Model updating is carried out by incorporating the gradients in the L-BFGS inversion algorithm (Nocedal and Wright, 2006).

It is relatively straightforward to extend the proposed VTI IDT algorithm to 3D. The separable dispersion relation (equation 1) remains valid in 3D if the wavenumber k_x is replaced with $k_r = \sqrt{k_x^2 + k_y^2}$ (Schleicher and Costa, 2016). 3D tomography requires generating additional image extensions (Sava and Vasconcelos, 2011), which is computationally expensive. The efficiency of the algorithm, however, can be increased by operating with common-image-point (CIP) gathers computed at sparse spatial locations (Yang and Sava, 2015).

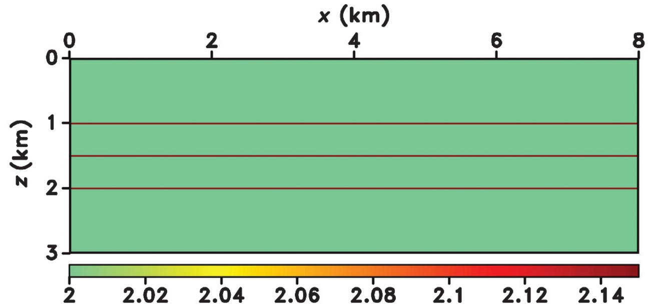

Figure 2. Constant-background VTI model with three horizontal perturbations in V_{nmo} at depths of 1, 1.5, and 2 km; $\eta = 0.15$, $\delta = 0.1$. The wavefield is generated by 21 sources evenly spaced between 0 and 4 km; the maximum offset is 2 km.

HORIZONTALLY LAYERED MODEL

First, we demonstrate on a simple model that nonstationary matching filters are capable of mitigating illumination-related artifacts in extended images. The model includes three horizontal interfaces (formed by perturbations in V_{nmo}), which are embedded in a homogeneous VTI background (Figure 2). The wavefield is excited by 21 sources evenly spaced at the surface. Figure 3 shows space-lag CIGs computed for a distorted model, in which η is set to zero (actual $\eta = 0.15$) and V_{nmo} is reduced by 10%. The CIGs contain three types of residual energy:

- the main energy-focusing point is shifted away from zero lag because of the error in V_{nmo} (see the yellow circles in Figure 3a).
- there is a "linear" energy defocusing caused by the distortion in η (Li et al., 2016a; Sava and Alkhalifah, 2012) (marked by the magenta ellipses in Figure 3b).
- there are aperture-truncation artifacts which are most pronounced near the surface (marked by the dashed lines in Figure 3c).

Defocusing due to aperture truncation is particularly visible in the "blurred" gathers obtained after applying the demigration

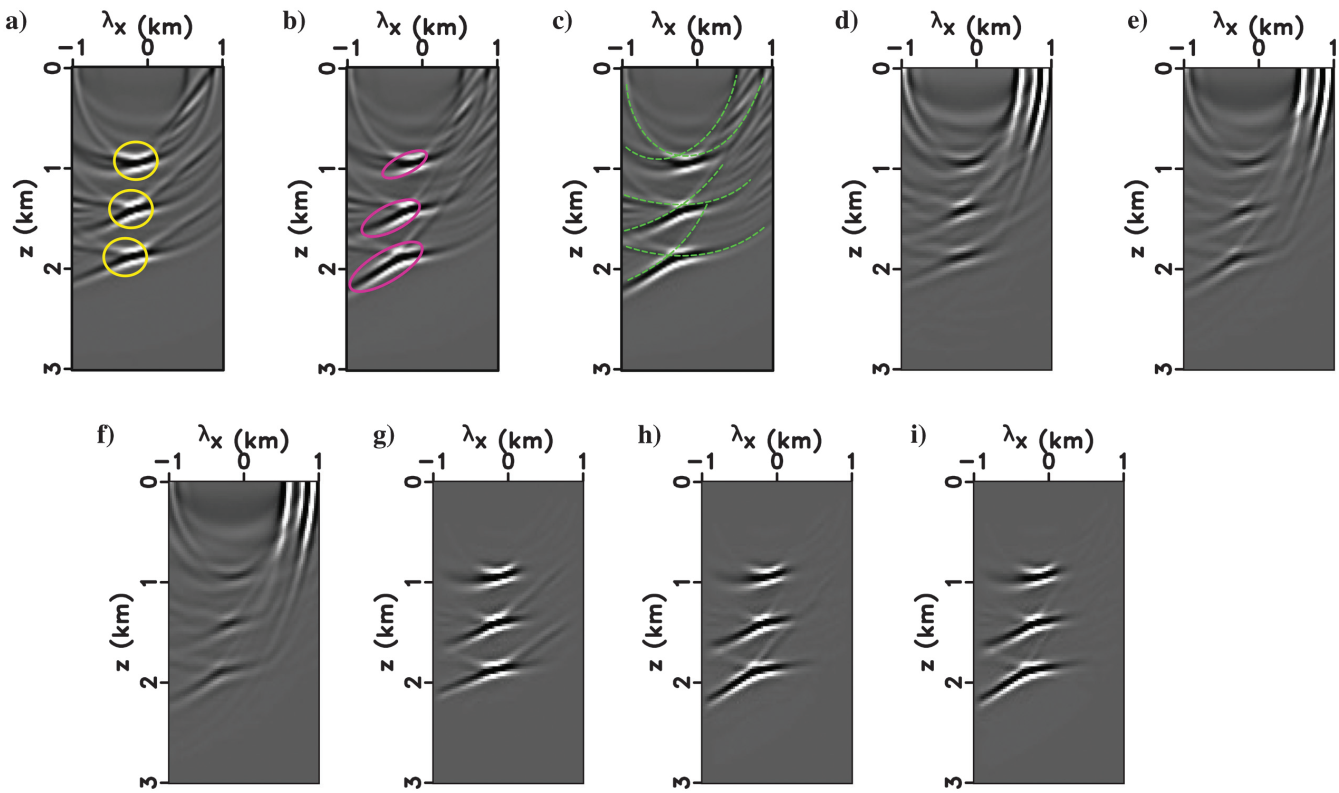

Figure 3. Extended images for the model in Figure 2 with $\eta = 0$ and V_{nmo} reduced by 10%. Each column corresponds to a different horizontal coordinate: (a,d,g) 1 km, (b,e,h) 2 km, and (c,f,i) 3 km. Plots (a-c) show the cross-correlation RTM gathers, (d-f) are the gathers after demigration and migration, and (g-i) are the gathers after applying the matching filters. The influence of V_{nmo}- and η-errors is indicated by the yellow circles and magenta ellipses, respectively. The green dashed lines mark the aperture-truncation artifacts.

and migration operators (Figure 3d–3f). The matching filters substantially mitigate the aperture-truncation artifacts without distorting the "useful" residuals caused by the errors in V_{nmo} and η (Figure 3g–3i).

MARMOUSI MODEL

Next, we test the algorithm on the VTI Marmousi-II model shown in Figure 4 (Guitton and Alkhalifah, 2016). The data consist of 100 shot gathers produced with an elastic finite-difference operator. We use the "streamer" acquisition geometry with the maximum offset equal to 6 km. To constrain the depth scale of the model, the parameter δ is assumed to be known at two "borehole" locations (Figure 4a).

The initial model is isotropic and weakly laterally heterogeneous; it is obtained by applying strong smoothing to the actual V_{nmo}-field

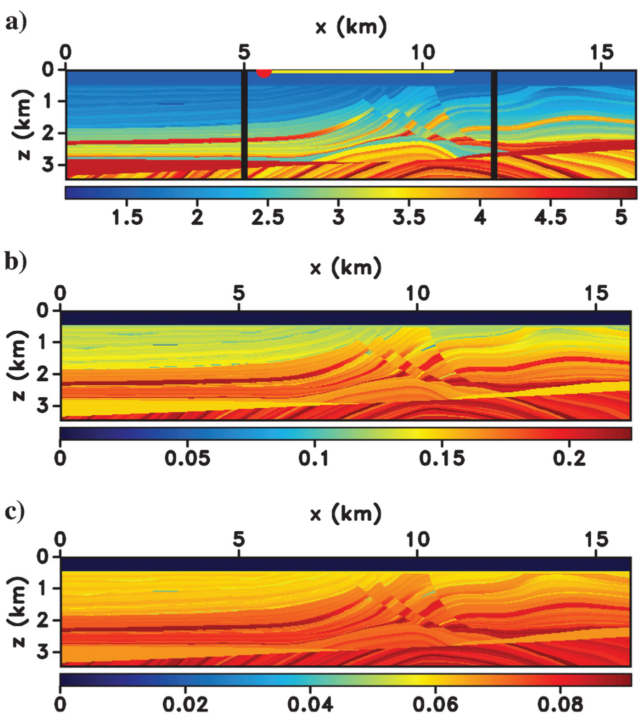

Figure 4. Parameters of the elastic VTI Marmousi-II model: (a) V_{nmo}, (b) η, and (c) δ. The vertical black lines on plot (a) mark the "borehole" locations where δ-profiles are available. 100 sources (one of them is marked by a red dot) are evenly spaced at the surface between 0 and 12 km. For each source location, the data are recorded by a "streamer" array (one of them is marked by the yellow line) with a maximum offset of 6 km.

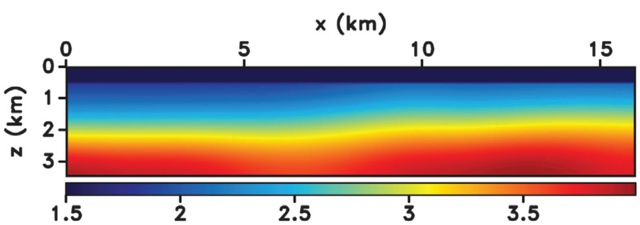

Figure 5. Initial isotropic velocity model obtained by smoothing the actual V_{nmo}-field.

(Figure 5). The extended RTM image computed with the initial model is significantly defocused due to velocity errors, as well as uneven illumination and aperture truncation (Figure 6). Two iterations of extended LSRTM substantially improve the image (Figure 7), which is then used in guided interpolation between the boreholes to obtain the initial δ-field. Imaging with the interpolated δ-field helps improve the spatial positioning of the migrated reflectors. Then the sequence of LSRTM and guided interpolation is applied for a second time to refine the spatial distribution of δ (Figure 8). The parameter δ is used primarily to ensure an accurate depth scale of migrated images, which could be accomplished with an interpolated δ-field that has a lower resolution than that in Figure 8.

Estimation of the parameters V_{nmo} and η is carried out using the three-stage IDT algorithm described above. The inner loop of the algorithm includes two iterations of the preconditioned extended LSRTM. Whereas the parameters V_{nmo} and η are computed by back-projecting the image residuals, the δ-field is obtained from image-guided interpolation and kept fixed at each inversion stage.

Because the initial model is highly inaccurate, it is not feasible to estimate V_{nmo} and η simultaneously without improving the V_{nmo}-field (Wang and Tsvankin, 2013b). In the shallow region, the overestimated V_{nmo} produces negative updates in η, thus moving the parameter search in the wrong direction. Therefore, at the first inversion stage, we update only V_{nmo} and set the factor α in the objective function (equation 8) to 0.5, which assigns a larger weight to the DSO term. After two model updates, the V_{nmo}-field is sufficiently improved (Figure 9) to focus energy in the extended gathers closer to zero lag (Figure 10) and make η-estimation possible.

The second inversion stage is designed to update only η using the elliptic ($\eta = 0$) velocity model obtained after stage 1. The factor α in equation 8 is set to unity to assign equal weights to both objective-function terms, which helps stabilize the η-updates. To increase the robustness of the η-estimation, strong image-guided smoothing is applied to the η-gradient.

After two iterations, the algorithm does not refine η anymore. The higher accuracy of the updated η-field (Figure 11) improves event focusing in the extended gathers (Figure 12). Image-guided

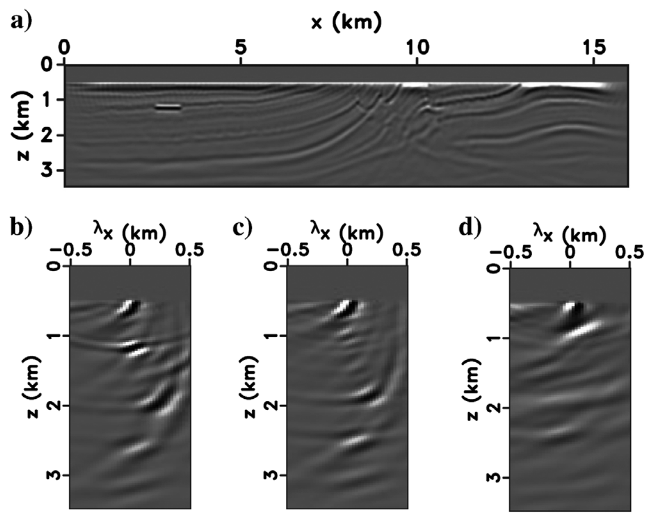

Figure 6. RTM output for the model from Figure 4 computed with the initial isotropic velocity field. (a) The conventional image and (b-d) the space-lag gathers at (b) 3 km, (c) 5 km, and (d) 9 km.

smoothing is instrumental in resolving the strongly anisotropic layer to the left of the faulted area at a depth of 2 km. However, η remains largely unconstrained below 3 km, which is due to relatively small offset-to-depth ratios and increasing errors in the NMO velocity with depth.

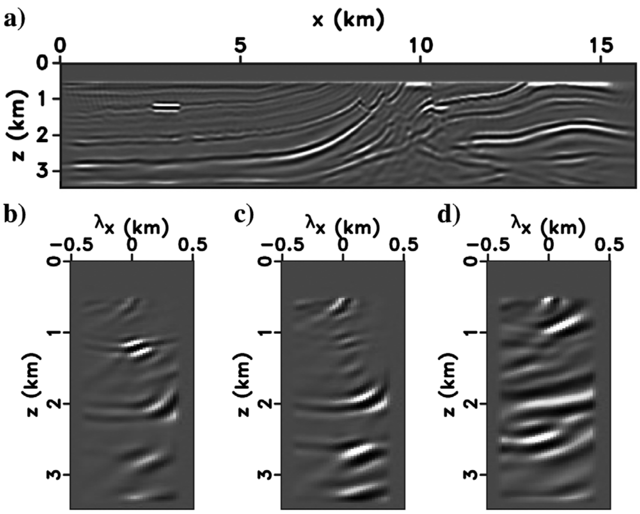

Figure 7. LSRTM output for the model from Figure 4 computed with the initial isotropic velocity field. (a) The conventional image and (b-d) the space-lag gathers at (b) 3 km, (c) 5 km, and (d) 9 km.

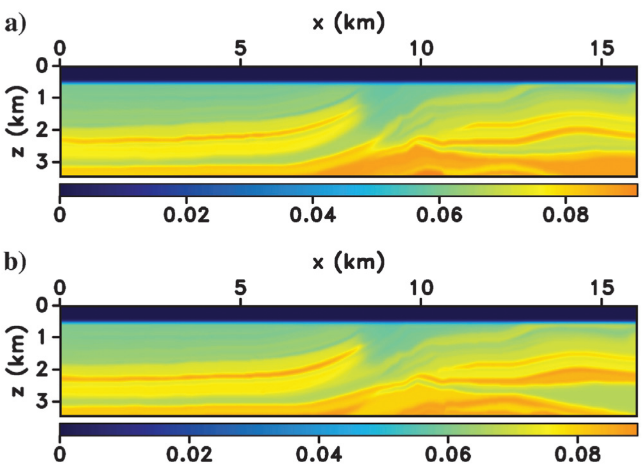

Figure 8. Initial δ-fields obtained by guided interpolation between the boreholes in Figure 4a using (a) the "purely isotropic" LSRTM image and (b) the refined image.

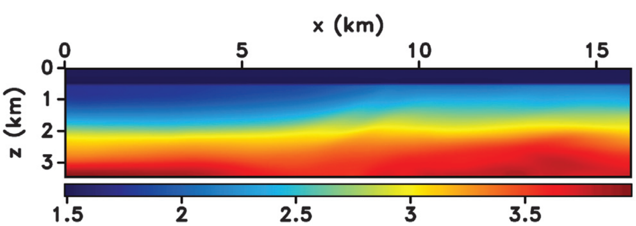

Figure 9. NMO velocity after stage 1 of the inversion.

With the more accurate V_{nmo}- and η-fields, at the third inversion stage we update the two parameters simultaneously and also invert for higher model-wavenumber components. The factor α is set to two to emphasize the IP term in the objective function. We also

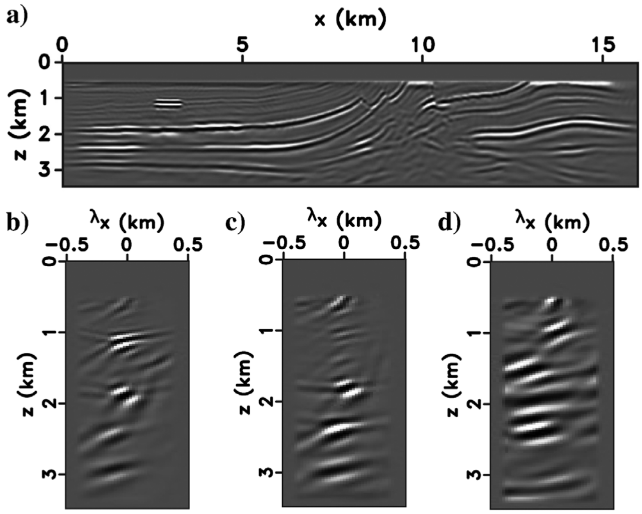

Figure 10. LSRTM output for the model from Figure 4 computed with the updated elliptic ($\eta = 0$) model. (a) The conventional image and (b-d) the space-lag gathers at (b) 3 km, (c) 5 km, and (d) 9 km.

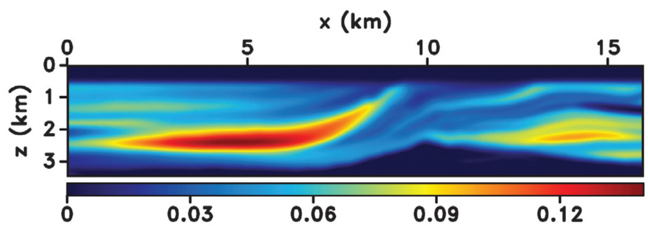

Figure 11. Parameter η after stage 2 of the inversion.

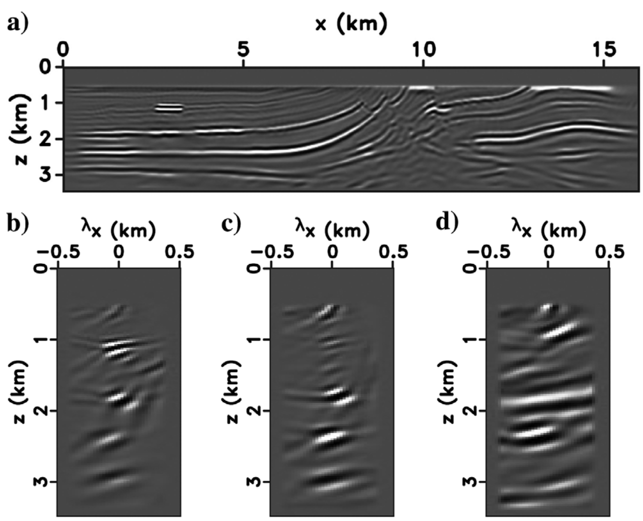

Figure 12. LSRTM output for the model from Figure 4 after stage 2. (a) The conventional image and (b-d) the space-lag gathers at (b) 3 km, (c) 5 km, and (d) 9 km.

relax the smoothing constraints but still apply stronger image-guided smoothing to the η-gradient compared to that for V_{nmo}. This is justified by the fact that reflection data help reconstruct V_{nmo} with a higher spatial resolution than η. Two more model updates add higher-contrast features to the V_{nmo}-field and slightly increase the resolution of η (Figure 13). These updates, however, provide only a marginal improvement in the focusing of the migrated events (Figure 14).

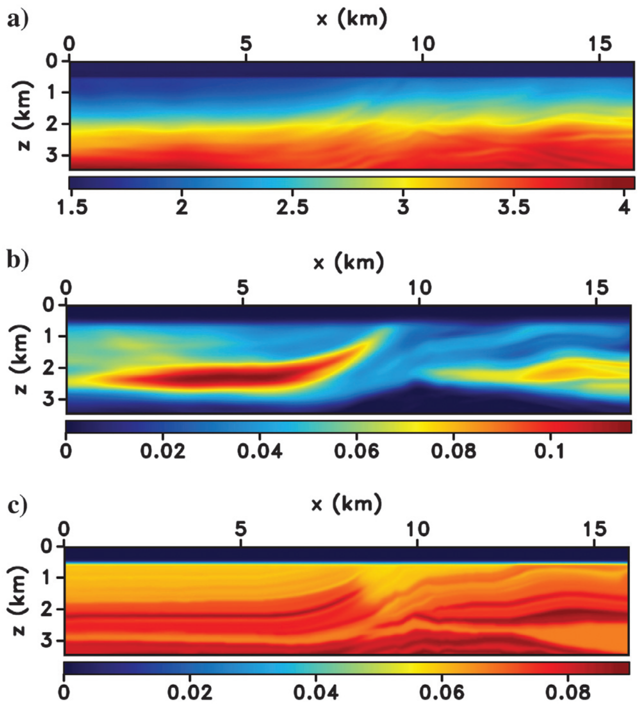

Figure 13. Final inverted parameters for the model from Figure 4: (a) V_{nmo}, (b) η, and (c) δ.

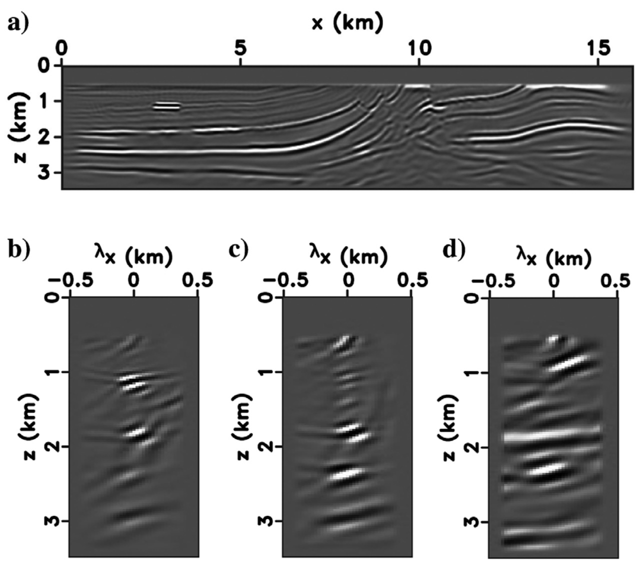

Figure 14. Final LSRTM output for the model from Figure 4. (a) The conventional image and (b-d) the space-lag gathers at (b) 3 km, (c) 5 km, and (d) 9 km.

GULF OF MEXICO DATA SET

Here, we present inversion results for a line from a 3D ocean-bottom-node (OBN) data set acquired in the Gulf of Mexico (courtesy of Shell). Preprocessing includes data projection onto the line, debubbling, P-Z summation, and normalization with a smooth data envelope that increases the amplitudes of the deeper events. The initial model provided by Shell is elliptic ($\eta = 0$) and features a salt dome embedded in subhorizontal sediment layers (Figure 15). We smooth the edges of the salt body to increase the robustness of imaging and suppress diffractions. To compensate for the relative sparseness of the OBN data, the mirror imaging technique (Figure 15a) is employed to increase the illumination.

The matching filters discussed above (Guitton, 2017) are used to precondition the first two LSRTM iterations. Application of LSRTM mitigates low-frequency artifacts caused by back-scattering from the ocean bottom and salt body and increases the amplitudes of the deeper reflections (Figure 16–16d).

The first inversion stage is designed to update the NMO velocity while keeping η fixed. However, updating V_{nmo} in this case study proved to be difficult due to the acquisition geometry of the OBN data. The sensitivity kernels of V_{nmo} are strongly influenced by the vertical wavenumbers, and, therefore, summation of the individual V_{nmo}-gradients over shots was hampered by the sparseness of the OBNs (exacerbated by the 2D limitation of our algorithm). Also, relatively weak defocusing in extended gathers (Figure 16b–16d) computed with the initial model indicate that the provided V_{nmo}-field may be sufficiently accurate.

In contrast, the sensitivity kernels of η mainly involve horizontal wavenumbers, so the quality of summation of the η-gradients over shots is less degraded because of the sparseness of the acquisition geometry. Hence, we start the inversion with stage 2 designed to update only η; the weighting factor α in equation 8 is set to unity.

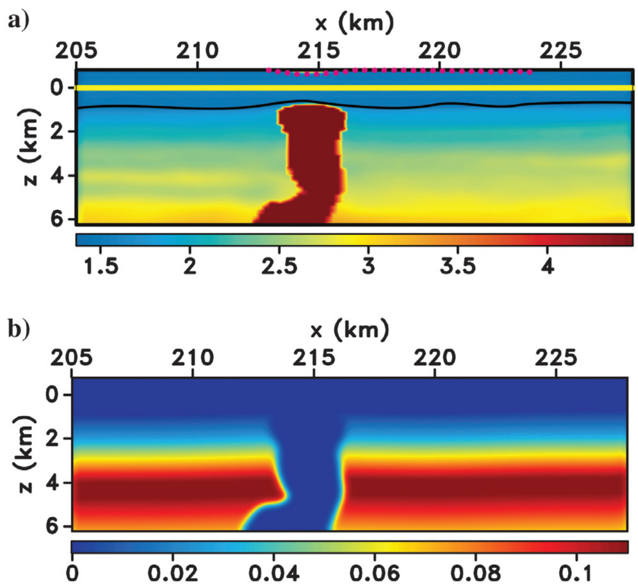

Figure 15. Initial elliptic ($\eta = 0$) model for the line from the Gulf of Mexico: (a) V_{P0} (with mirror geometry used for imaging and tomography) and (b) $\delta = \epsilon$. The yellow line marks the water surface and the magenta dots represent ocean-bottom nodes mirrored with respect to the water bottom (black line).

As discussed above, if the vertical profiles of the parameter δ are available at borehole locations, the δ-field can be built through image-guided interpolation. Likewise, in this case study image-guided interpolation using updated migrated sections potentially could help refine the provided δ-model. However, because most interfaces are subhorizontal, changes in the parameter η during the inversion hardly influence the positioning of migrated reflectors. Hence, image-guided interpolation could not be used to update the δ-field, and we kept this parameter fixed.

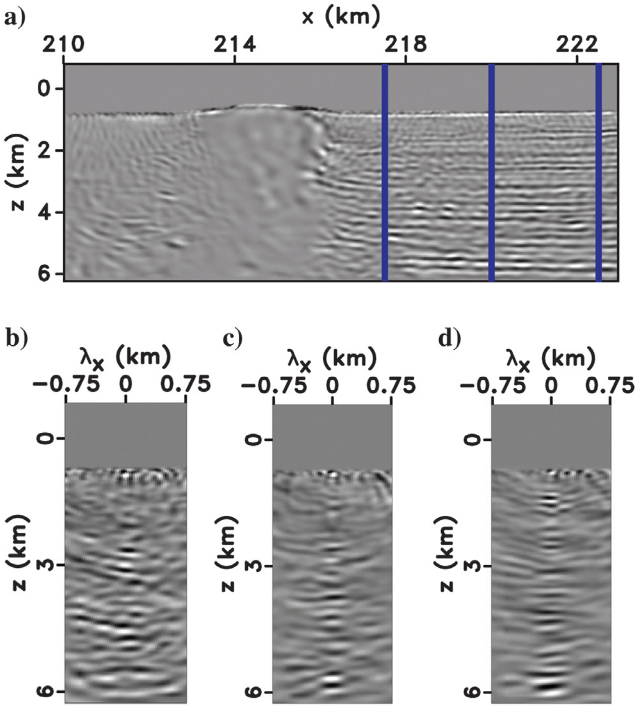

Figure 16. LSRTM output for the Gulf of Mexico data using the initial model from Figure 15. (a) The conventional image and (b-d) the space-lag gathers at the locations marked by the vertical blue lines after 16 iterations of LSRTM.

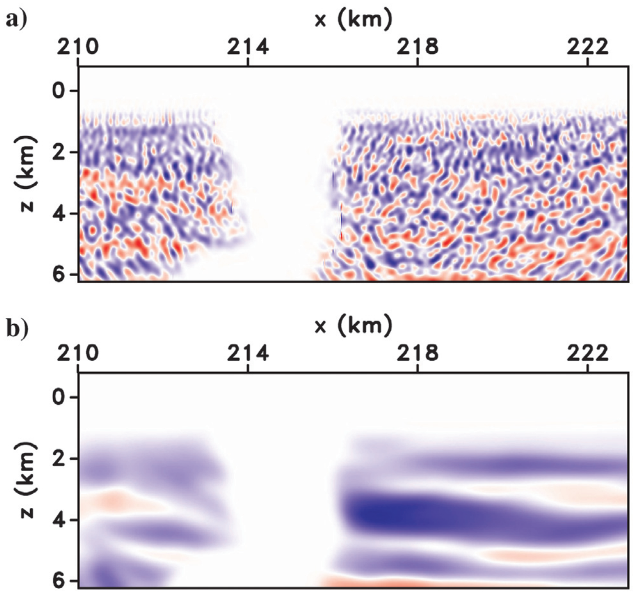

Figure 17. IDT gradient for η (a) before and (b) after preconditioning.

Preconditioning of the initial inversion gradient for η (Figure 17a) includes image-guided smoothing and smooth-envelope normalization with the goal of suppressing undesired high model-wavenumber components and enhancing the updates in the deeper part of the model (Figure 17b). We also set η to zero in the water and salt body. In addition, the η-gradient is scaled by the δ-field (normalized by the maximum value of δ) to enforce the similarity between the updated parameters η and δ. This procedure is justified by the fact that η and δ are often correlated (Wang, 2002).

The first iteration of IDT produces positive η-updates (the initial $\eta = 0$) reaching the maximum values close to 0.06 at a depth of 4 km (Figure 18). The inverted η-field provides some image improvements (compare Figure 16a with Figure 19a) and a 15% reduction in the

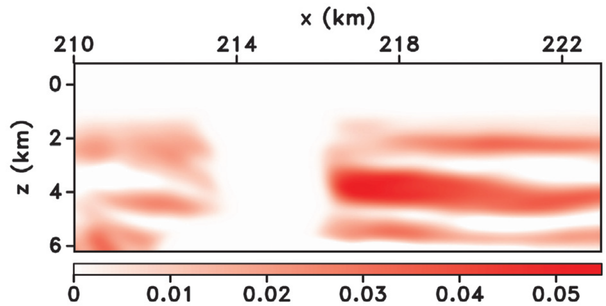

Figure 18. Updated η-field after stage 2 of the inversion.

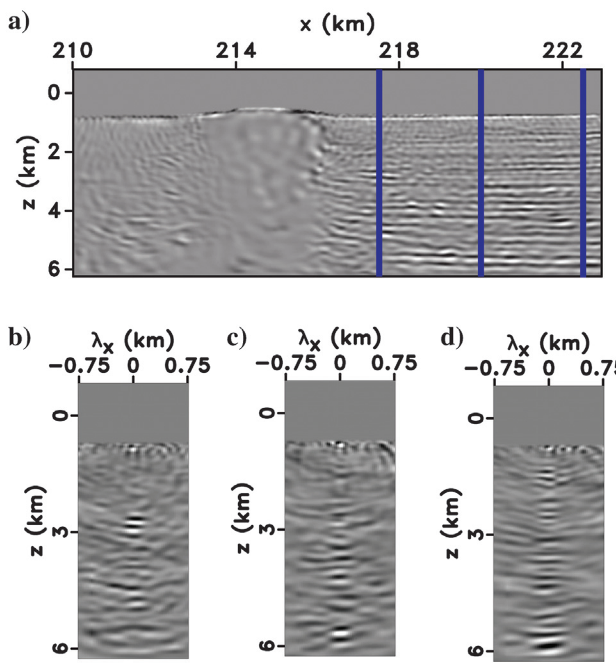

Figure 19. LSRTM output for the Gulf of Mexico data using the updated η-field. (a) The conventional image and (b-d) the space-lag gathers at the locations marked by the vertical blue lines after 16 iterations of LSRTM.

IDT objective function. It is possible that the initial V_{nmo}-field is slightly overestimated, which reduces the magnitude of η-updates. Further improvement in the η-field could be obtained by inverting for V_{nmo} and η simultaneously (third stage of IDT), which was not feasible in this case study because of the sparseness of the acquisition geometry (see above).

CONCLUSIONS

We presented an acoustic image-domain tomographic algorithm designed to reconstruct P-wave VTI velocity models using wave-equation imaging. Least-squares reverse time migration (LSRTM) plays a crucial role in mitigating aperture- and illumination-induced artifacts in the extended domain. Application of nonstationary matching filters facilitates the convergence of LSRTM and significantly improves the efficiency of the entire IDT algorithm. The three-stage inversion strategy mitigates the trade-off between the normal-moveout velocity V_{nmo} and anellipticity parameter η, and image-guided smoothing steers the algorithm towards geologically plausible solutions. The Thomsen parameter δ is reconstructed from image-guided interpolation between available boreholes. The high computational cost of the inner-loop LSRTM is partly compensated by a small number of outer-loop iterations.

The algorithm was applied to the elastic VTI Marmousi-II model starting from a purely isotropic, substantially distorted velocity field. The updates in V_{nmo}, η, and δ obtained after six iterations of IDT significantly improved the LSRTM image. The inversion results for a line from the Gulf of Mexico suggest that the initial elliptic ($\eta = 0$) model can be improved with positive η-updates. The robustness of field-data applications can be increased by extending the algorithm to 3D which, however, remains prohibitively expensive. Ongoing work includes a generalization of the method for tilted TI media.

ACKNOWLEDGMENTS

This work was supported by the Consortium Project on Seismic Inverse Methods for Complex Structures at CWP and competitive research funding from King Abdullah University of Science and Technology (KAUST). We are grateful to Shell Exploration and Production Company for sharing the 3D Gulf of Mexico data set with Colorado School of Mines, and for their permission to publish the field-data results. We also thank Daniel Rocha (CWP) for his help in preprocessing the data. The numeric examples in this paper are generated with the Madagascar open-source software package (Fomel et al., 2013a) freely available from http://www.ahay.org.

DATA AND MATERIALS AVAILABILITY

All data used in this paper except for the dataset from the Gulf of Mexico (Courtesy of Shell) are available. The Gulf of Mexico data are confidential (property of Shell).

REFERENCES

Alkhalifah, T., 1998, Acoustic approximations for processing in transversely isotropic media: Geophysics, **63**, 623–631, doi: 10.1190/1.1444361.

Alkhalifah, T., 2000, An acoustic wave equation for anisotropic media: Geophysics, **65**, 1239–1250, doi: 10.1190/1.1444815.

Chauris, H., and E. Cocher, 2017, From migration to inversion velocity analysis: Geophysics, **82**, no. 3, S207–S223, doi: 10.1190/geo2016-0359.1.

Chavent, G., and C. A. Jacewitz, 1995, Determination of background velocities by multiple migration fitting: Geophysics, **60**, 476–490, doi: 10.1190/1.1443785.

Clément, F., G. Chavent, and S. Gómez, 2001, Migration-based traveltime waveform inversion of 2D simple structures: A synthetic example: Geophysics, **66**, 845–860, doi: 10.1190/1.1444974.

Dafni, R., and W. W. Symes, 2016, Kinematic artifacts in the subsurface-offset extended image and their elimination by a dip-domain specularity filter: Geophysics, **81**, no. 6, S477–S495, doi: 10.1190/geo2016-0115.1.

Du, X., P. J. Fowler, and R. P. Fletcher, 2014, Recursive integral time-extrapolation methods for waves: A comparative review: Geophysics, **79**, no. 1, T9–T26, doi: 10.1190/geo2013-0115.1.

Fomel, S., P. Sava, I. Vlad, Y. Liu, and V. Bashkardin, 2013a, Madagascar: Open-source software project for multidimensional data analysis and reproducible computational experiments: Journal of Open Research Software, **1**, e8.

Fomel, S., L. Ying, and X. Song, 2013b, Seismic wave extrapolation using lowrank symbol approximation: Geophysical Prospecting, **61**, 526–536, doi: 10.1111/j.1365-2478.2012.01064.x.

Guitton, A., 2017, Fast 3D least-squares RTM by preconditioning with nonstationary matching filters: 87th Annual International Meeting, SEG, Expanded Abstracts, 4395–4399, doi: 10.1190/segam2017-17588457.1.

Guitton, A., and T. Alkhalifah, 2016, An optimal parameterization for full waveform inversion in anisotropic media: 78th Annual International Conference and Exhibition, EAGE, Extended Abstracts, doi: 10.3997/2214-4609.201601192.

Guitton, A., G. Ayeni, and E. Díaz, 2012, Constrained full-waveform inversion by model reparameterization: Geophysics, **77**, no. 2, R117–R127, doi: 10.1190/geo2011-0196.1.

Hale, D., 2009a, Image-guided blended neighbor interpolation of scattered data: 79th Annual International Meeting, SEG, Expanded Abstracts, 1127–1131, doi: 10.1190/1.3255050.

Hale, D., 2009b, Structure-oriented smoothing and semblance: CWP Project Review Report, 635, 1–10.

Hicks, G. J., and R. G. Pratt, 2001, Reflection waveform inversion using local descent methods: Estimating attenuation and velocity over a gas-sand deposit: Geophysics, **66**, no. 2, 598–612, doi: 10.1190/1.1444951.

Hou, J., and W. W. Symes, 2017, An alternative formula for approximate extended born inversion: Geophysics, **82**, no. 1, S1–S8, doi: 10.1190/geo2016-0327.1.

Lameloise, C.-A., H. Chauris, and M. Noble, 2015, Improving the gradient of the image-domain objective function using quantitative migration for a more robust migration velocity analysis: Geophysical Prospecting, **63**, 391–404, doi: 10.1111/1365-2478.12195.

Li, V., I. Tsvankin, and T. Alkhalifah, 2016a, Analysis of RTM extended images for VTI media: Geophysics, **81**, no. 3, S139–S150, doi: 10.1190/geo2015-0384.1.

Li, V., H. Wang, I. Tsvankin, E. Díaz, and T. Alkhalifah, 2017, Inversion gradients for acoustic VTI wavefield tomography: Geophysics, **82**, no. 4, WA55–WA65, doi: 10.1190/geo2016-0624.1.

Li, Y., B. Biondi, R. Clapp, and D. Nichols, 2016b, Integrated VTI model building with seismic data, geologic information, and rock-physics modeling — Part 1: Theory and synthetic test: Geophysics, **81**, no. 5, C177–C191, doi: 10.1190/geo2015-0592.1.

Ma, Y., D. Hale, B. Gong, and Z. J. Meng, 2012, Image-guided sparse-model full waveform inversion: Geophysics, **77**, no. 4, R189–R198, doi: 10.1190/geo2011-0395.1.

Mulder, W., 2014, Subsurface offset behaviour in velocity analysis with extended reflectivity images: Geophysical Prospecting, **62**, 17–33, doi: 10.1111/1365-2478.12073.

Nocedal, J., and S. J. Wright, 2006, Numerical optimization, 2nd ed.: Springer-Verlag.

Pattnaik, S., I. Tsvankin, H. Wang, and T. Alkhalifah, 2016, Full-waveform inversion with reflected waves for 2D VTI media: 86th Annual International Meeting, SEG, Expanded Abstracts, 413–418, doi: 10.1190/segam2016-13967833.1.

Rickett, J., and P. Sava, 2002, Offset and angle-domain common image-point gathers for shot-profile migration: Geophysics, **67**, 883–889, doi: 10.1190/1.1484531.

Sava, P., and T. Alkhalifah, 2012, Anisotropy signature in extended images from reverse-time migration: 82nd Annual International Meeting, SEG, Expanded Abstracts, doi: 10.1190/segam2012-0124.1.

Sava, P., and S. Fomel, 2003, Angle-domain common-image gathers by wavefield continuation methods: Geophysics, **68**, 1065–1074, doi: 10.1190/1.1581078.

Sava, P., and I. Vasconcelos, 2009, Efficient computation of extended images by wavefield-based migration: 79th Annual International Meeting, SEG, Expanded Abstracts, 2824–2828, doi: 10.1190/1.3255436.

Sava, P., and I. Vasconcelos, 2011, Extended imaging conditions for wave-equation migration: Geophysical Prospecting, **59**, 35–55, doi: 10.1111/j.1365-2478.2010.00888.x.

Schleicher, J., and J. C. Costa, 2016, A separable strong-anisotropy approximation for pure qP-wave propagation in transversely isotropic media: Geophysics, **81**, no. 6, C337–C354, doi: 10.1190/geo2016-0138.1.

Shan, G., and Y. Wang, 2013, RTM based wave equation migration velocity analysis: 83rd Annual International Meeting, SEG, Expanded Abstracts, 4726–4731, doi: 10.1190/segam2013-0665.1.

Shan, G., Y. Wang, and U. Albertin, 2014, Wave equation migration velocity analysis by wavefield decomposition: 84th Annual International Meeting, SEG, Expanded Abstracts, 4680–4685, doi: 10.1190/segam2014-1112.1.

Shen, P., and W. W. Symes, 2008, Automatic velocity analysis via shot profile migration: Geophysics, **73**, no. 5, VE49–VE59, doi: 10.1190/1.2972021.

Soubaras, R., and B. Gratacos, 2007, Velocity model building by semblance maximization of modulated-shot gathers: Geophysics, **72**, no. 5, U67–U73, doi: 10.1190/1.2743612.

Symes, W. W., and J. J. Carazzone, 1991, Velocity inversion by differential semblance optimization: Geophysics, **56**, 654–663, doi: 10.1190/1.1443082.

Tsvankin, I., 2012, Seismic signatures and analysis of reflection data in anisotropic media, 3rd ed.: SEG.

Wang, X., and I. Tsvankin, 2013a, Ray-based gridded tomography for tilted transversely isotropic media: Geophysics, **78**, no. 1, C11–C23, doi: 10.1190/geo2012-0066.1.

Wang, X., and I. Tsvankin, 2013b, Multiparameter TTI tomography of P-wave reflection and VSP data: Geophysics, **78**, no. 5, WC51–WC63, doi: 10.1190/geo2012-0394.1.

Wang, Z., 2002, Seismic anisotropy in sedimentary rocks, part 2: Laboratory data: Geophysics, **67**, 1423–1440, doi: 10.1190/1.1512743.

Weibull, W. W., and B. Arntsen, 2014, Anisotropic migration velocity analysis using reverse-time migration: Geophysics, **79**, no. 1, R13–R25, doi: 10.1190/geo2013-0108.1.

Yang, T., and P. Sava, 2015, Image-domain wavefield tomography with extended common-image- point gathers: Geophysical Prospecting, **63**, 1086–1096, doi: 10.1111/1365-2478.12204.

Zhang, Y., and G. Shan, 2013, Wave-equation migration velocity analysis using partial stack-power maximization: 83rd Annual International Meeting, SEG, Expanded Abstracts, 4847–4852, doi: 10.1190/segam2013-0716.1.